Original Article
Establishment of patient-derived xenograft models of adenoid cystic carcinoma to assess pre-clinical efficacy of combination therapy of a PI3K inhibitor and retinoic acid

Bao Sun[1,2,3*], Yu Wang[1,2,3*], Jingjing Sun[1,2,3], Chunye Zhang[1,2,3], Ronghui Xia[1,2,3], Shengming Xu[2,3,4], Shuyang Sun[2,3,4], Jiang Li[1,2,3]

[1]Department of Oral Pathology, Shanghai Ninth People's Hospital, College of Stomatology, Shanghai Jiao Tong University School of Medicine, Shanghai 200011, P. R. China; [2]National Clinical Research Center for Oral Diseases, Shanghai 200011, P. R. China; [3]Shanghai Key Laboratory of Stomatology & Shanghai Research Institute of Stomatology, Shanghai 200011, P. R. China; [4]Department of Oral and Maxillofacial-Head & Neck Oncology, Ninth People's Hospital, Shanghai Jiao Tong University School of Medicine, Shanghai 200011, P. R. China. *Equal contributors.

Abstract: Due to the difficulties and long periods of establishment, preclinical animal models of adenoid cystic carcinoma (ACC) are scarce but imperative. The researches involving molecular features and therapeutic targets of ACC require an integrated group of preclinical animal models which can credibly retain the heterogeneity of this tumor. Currently chemotherapies and targeting therapies have modest efficacy in ACC and the overall response rate is rather low. Therefore, novel therapeutic regimen of ACC is urgently needed and remains a major clinical challenge. We transplanted a group of tumor samples from human salivary ACC into immunodeficient mice to establish patient-derived xenografts (PDXs). Patient tumors and their matched PDXs were conducted histological analyses, whole-exome sequencing (WES) and RNA-seq respectively. 13 PDXs were successfully established from 34 ACC, involved in 3 histological types, including cribriform, tubular, and solid. These ACC PDXs generally reflected the histopathological and molecular features of their corresponding original tumors. MYB/MYBL1-NFIB fusion (53.85%) and high-frequency mutation genes, such as KDM6A, KMT2C, KMT2D, NOTCH1, NOTCH2, SMARCA4 and PIK3CA were mainly conserved in PDXs. Guided by the genetic alterations, the efficiencies of retinoic acid (RA) and a PI3K inhibitor were evaluated in ACC PDX models harboring both MYB fusion and PIK3CA amplification/mutation. Combination treatment of the PI3K inhibitor and RA demonstrated remarkable inhibition of tumors in PDXs harboring both PIK3CA mutation/amplification and MYB-NFIB fusion gene in vivo and in vitro. In this study, we displayed the morphologically and genetic featured PDXs which recapitulated the heterogeneity of original ACC tumors, indicating that the models could be used as a platform for drug screening for therapy response. The feasibility of combination treatment approaches for dual targets were confirmed, providing new regimens for personalized therapies in ACC.

Keywords: Adenoid cystic carcinoma, patient-derived xenograft, WES, targeting therapy, PI3K inhibitor, retinoic acid

Introduction

Adenoid cystic carcinoma (ACC) is among the most prevalent salivary malignancies, and also occurred in breast, lung and lacrimal gland, etc. Although ACC exhibits indolent growth, it has a confirmed propensity for aggressive perineural invasion and high rates of distant metastasis, which ultimately result in low survival rates and poor prognosis [1]. In histomorphology,

ACC consists of typical glandular epithelial and myoepithelial cells, which arrange in cribriform, tubular and solid patterns with abundant hyaline extracellular secretion [2]. High-grade ACC, with substantial solid components in the tumor, is associated with a more advanced stage and more prefer to distant metastases [3]. Current treatments are still mainly surgery and adjuvant radiation, and no systemic chemotherapy has been proven to be fully effective [4]. The mecha-

nisms involved in ACC are still poorly understood. One important genetic alteration in ACC is the recurrent t(6;9) (q22-23; p23-24) translocation, which is considered as a hallmark in the pathogenesis of this disease and results in a fusion gene named MYB-NFIB [5, 6]. This fusion gene has been reported in over 50% of ACCs and results in overexpression of MYB protein, suggesting that MYB may be a potential therapeutic target for ACC [7]. Previous evidence indicated that retinoic acid restrained MYB expression, possibly by interrupting MYB-driven transcriptional regulation [8]. At present, clinical trials using all-trans retinoic acid has being recruited for patients with confirmed advanced, recurrent/metastatic ACC (Clinical Trials.gov: NCT04433169).

On account of the complexity of this disease process and the unclear etiology, no standard treatment regimen has been designed for ACC, which still consists of surgery and radiotherapy [9]. There is no recommended specific chemotherapeutic regimen and conventional chemotherapeutic regimens, such as cisplatin and doxorubicin, remain being used in clinical treatments [10]. Consideration of the modest efficacy of current chemotherapies in ACC, therapies targeting various molecular have applied to clinical trials in an aim to improve the long-term prognosis of patients. NOTCH1 mutation has been defined as a distinct group characterized by solid histology, distant metastasis, and poor prognosis [11]. Recently, clinical trials targeting NOTCH signaling (confirmed ACC with NOTCH1/2/3/4 activating mutation) in a genotype-defined ACC subgroup have being performed in a phase II clinical trial, which is still recruiting (Clinical Trials.gov: NCT03691207).

Overexpression of c-KIT has been reported in majority of ACCs, but inhibitors of c-KIT (e.g., dasatinib) are shown to be ineffective in a phase II clinical trial [12]. Drugs interfering epidermal growth factor receptor (EGFR), including cetuximab, gefitinib or lapatinib, did not obtain objective responses, but some patients attained prolonged stabilization [13-15]. Moreover, other clinical trials involving targeted therapies for FGFR (fibroblast growth factor receptor, FGFR), HER2 and VEGFR (vascular endothelial growth factor receptor, VEGFR) showed partial response [16-18]. Single agent, either in clinical trials or basic research, has not yielded active results yet. Effective combined thera-

peutic regimen is required to improve long-term outcomes for ACC patients currently.

The conventional cancer cell lines and animal models fail to accurately recapitulate intratumor heterogeneity of ACC. ACC PDXs faithfully retain the morphological and genetic characteristics of the original tumors and have promoted the progress of the preclinical and translational research [19]. PDX models are established by subcutaneous implantation of small pieces of patient tumors into immunodeficient mice, which are propagated to obtain cohorts of animals bearing tumors from patients. In addition, tumor biological markers can be identified and then preclinical trials can be performed though PDXs to evaluate the responses to targeted drugs [20]. Indeed, several studies in PDX models of ACC generated important preclinical information that led to the further execution of clinical trials. Felipe Nör et al demonstrated that a small molecule (MI-773) interrupted MDM2-p53 interaction and sensitized to cisplatin in low-passage primary human ACC models [21]. Knowledge about the underlying genomic landscape of ACC is needed to understand, leading to the development of effective therapies in future.

Here, we provided genomic profiles of a panel of salivary ACC and established a group of PDX models. Through whole-exome sequencing (WES), bioinformatic analysis and histopathological verification, we found that the PDXs recapitulated the genetic stability of the matched primary tumors. Based on the previous results, a PI3K inhibitor was selected for combination efficacy evaluation with RA in PDXs and PDX-derived cells with PIK3CA amplification/mutation and MYB. In addition, combination of the PI3K inhibitor with conventional therapies were further assessed.

Materials and methods

Patient tumor sample preparations

Tumor collection and related studies were permitted by the Institutional Review Board and the Ethics Committee of Shanghai Ninth People's Hospital, Shanghai Jiao Tong University School of Medicine. After patients' informed permission, fresh specimens were acquired from patients undergoing surgical resection without radiotherapy or chemotherapy. All ACC

cases were diagnosed by at least two different pathologists.

Establishment of xenografts

Fresh tumors were obtained from ACC patients and immediately immersed in cold DMEM with 1% penicillin and streptomycin. After briefly processing, tumor tissues from patients were minced into small fragments (approximately 20-30 mm^3) and implanted into the flank region of BALB/c nude mice (female mice, about 4-5 weeks old) subcutaneously. When the volume reached approximately 1000 mm^3 (V = 0.5*ab^2, a refers to the largest tumor diameter and b refers to the shortest diameter), the tumors were harvested and passaged for subsequent implantation. Parts of the fresh patient tumors and passaged tumors were cryopreserved in liquid nitrogen and embedded in paraffin for histological analysis. All the above experiments were conducted under the permission and the supervision of the Institutional Animal Care and Use Committee (IACUC) of Shanghai Jiao Tong University School of Medicine.

Genomic analysis

Whole-exome sequencing: DNA from fresh-frozen tumor tissue, normal salivary gland tissue, blood or formalin-fixed and paraffin-embedded (FFPE) samples were isolated (DNeasy Blood and Tissue Kit, Cat# 69506, QIAGEN, USA) by utilizing standard previous methods. Genomic DNA (0.6 µg per sample) from each sample was prepared for sequencing. Sequencing libraries were produced by an Agilent SureSelect Human All Exon Kit V6 (Agilent Technologies, CA, USA) following the manufacturer's instructions. In brief, 180-280 bp fragments were obtained through a hydrodynamic shearing system (Covaris, Massachusetts, USA) and were connected to he joint to prepare the DNA libraries. The libraries were enriched and captured by PCR reaction and index tags were added to prepare for subsequent sequencing. The products were purified by an AMPure XP system (Cat# A63987, Beckman Coulter, CA) and then quantified through an Agilent High Sensitivity DNA Assay (Agilent 2100 Bioanalyzer System). Tumor and normal tissues were sequenced at 200× and 100× coverage, respectively.

Fusion gene identification: RNA from fresh-frozen human tissue samples was isolated and then was performed RNA-seq. The cDNA librar-

ies were constructed using the Illumina TruSeq for mRNA. The libraries were sequenced at 2×100 paired-end at a mean coverage of 100-200× depth in the annotated transcriptome.

Clustering and sequencing: The sample clustering was conducted through a cBot Cluster Generation System (Hiseq PE 150 Cluster Kit, Illumina, CA, USA) according to the manufacturer's recommendations. When clustering finished, the DNA libraries were sequenced by the Illumina HiSeq platform and then 150 bp paired-end reads were conducted.

To get the raw mapping results, the valid data of sequencing was mapped to the human reference genome (UCSC GRCh37/hg19) by Burrows-Wheeler Aligner software and the data was stored in BAM format. The somatic SNV was detected by muTect [22] and In/Dels were detected by Strelka [23]. Control-FREEC was applied to detect somatic CNV [24].

Detection of fusion gene transcripts

Total RNA from frozen fresh tissues was isolated with TRIzol reagent (Cat# 15596018, Invitrogen, USA) as previously described [25]. RNA was treated with DNase and reverse transcribed to cDNA according to the manufacturer's instructions. MYB-NFIB and NFIB-MAP3K5 fusion transcripts were detected by RT-PCR with Premix Taq DNA polymerase (RR902, Takara, Japan), and new primers were developed as listed below.

MYB-NFIB: Forward primer: TGGGAAGGGGAC-AGTCTGAA; Reverse primer: CTAGCCCAGGTA-CCAGGACT; NFIB-MAP3K5: Forward primer 1: CACCAAGCAGCAAAAGACCC; Reverse primer 1: CAGTGACTGCAGAGAGTCCG; Forward primer 2: CGGGGGTCAATCTTCAGAGG; Reverse primer 2: GTAAAACAAGGACGGCTGCC.

Histological staining

Rabbit polyclonal antibodies against human Ki67 (ab15580) and MYB (ab45150) were purchased from Abcam (Cambridge, UK). Antibodies for P63 (Gene Tech, Shanghai, China), CK19 (Dako, Carpinteria, CA), and Ki67 (Dako, Carpinteria, CA) were used in the following immunohistochemical (IHC) staining analysis. Both hematoxylin and eosin (H&E) and IHC staining were performed on FFPE tissue sections of tumors and PDXs. All specimens were sectioned (4 µm thick), dewaxed and rehydrated as previously reported [26]. After sections

were blocked with 3% H_2O_2, Tri-EDTA solution was used for antigen retrieval. Then, sections were incubated with anti-MYB (dilution ratio, 1:100), anti-Ki67 (dilution ratio, 1:100), anti-P63 (dilution ratio, 1:200), and anti-CK19 (dilution ratio, 1:200) antibodies diluted according to the instructions overnight at 4°C. A goat-anti rabbit secondary antibody (DAKO, Glostrup, Denmark) labeled by horseradish peroxidase (HRP) was then added at room temperature for 0.5 hour. Subsequently, HRP was visualized with DAB, and the nuclei were stained with hematoxylin.

Fluorescence in situ hybridization (FISH)

The MYB fusion status was assessed in FFEP tissue sections using a MYB Break Apart Dual Color Probe (ZTV-Z-2143-200; ZytoVision, Germany) according to the manufacturer's instructions. Pretreatment, including dewaxing and proteolysis, was performed as previously described. Denaturation was performed at 75°C for 10 min, and then slides were transferred to a humidified chamber for hybridization overnight at 37°C. The hybridization signals of the probe appeared as green fluorescence (close to the MYB breakpoint region) and red fluorescence (distal to the breakpoint region). A translocation is indicated by one separate green signal and one separate red signal (separated by a distance of >1 signal diameter). Isolated and intact cells with distinct boundaries were included and excluded overlapping cells. For each case, we counted at least 100 cells. A number of positive cells were over 30% of the total cell count indicated MYB gene abnormalities.

Drug efficacy evaluation in vivo

BALB/c nude mice were randomly divided into different treated groups when the tumors reached a mean volume of 80-100 mm³. Mice in the treated group were orally administered alpelisib (25 mg/kg), RA (40 mg/kg), cisplatin (5 mg/kg), and corn oil (as the control). Both alpelisib and RA were diluted in corn oil as previously reported [8]. The tumor size and weight were monitored twice weekly. After 28 days treatment, tumors were harvested, and a tumor growth curve was constructed. The inhibition effects (Tumor growth inhibition, TGI) were assessed as follows: $1 - [(Treated_{final} - Treated_{initial})/(Control_{final} - Control_{initial})]$.

Western blot

Alpelisib was purchased from MedChemExpress (HY-15244, USA). RA was purchased from Sigma-Aldrich (SIGMA-R2625, St. Louis, MO, USA). The antibodies used in this procedure were purchased from Cell Signaling Technology (CST, Danvers, MA, USA) and Abcam (CA, United States). AKT (CST, #4685), phospho-AKT (Ser473, CST, #4060), phospho-AKT (CST, Thr308, #13038), ERK1/2 (CST, #4695), phospho-ERK1/2 (CST, p-ERK1/2; Tyr202/Tyr204, #4370), P110α (CST, #4249), GAPDH (CST, #2118) and MYB (Abcam, ab217945).

Immunoblotting was performed according to standard SDS-PAGE protocols. In brief, proteins from tissues were extracted with lysis buffer, separated in SDS-PAGE gels (4%-20%) and then transferred to PVDF membranes. When blocked with 5% milk powder, membranes were incubated with antibodies against MYB (dilution ratio, 1:1000), P110α (dilution ratio, 1:1000), p-AKT (dilution ratio, 1:1000), AKT (dilution ratio, 1:1000), p-ERK (dilution ratio, 1:1000), ERK (dilution ratio, 1:1000) and GAPDH (dilution ratio, 1:1000) at 4°C overnight. Then, membranes above were incubated with a secondary anti-rabbit antibody (dilution ratio, 1:2500) at room temperature for 60 minutes. The chemiluminescence signals were captured through an Odyssey Infrared Imaging System following the recommendations.

Patient-derived xenograft cells

Tumor tissues from 019-PDX (harboring the PIK3CA^R88Q mutation) and 044-PDX (harboring PIK3CA amplification) were washed extensively with serum-free DMEM, minced into small pieces and dissociated in DMEM with collagenase/hyaluronidase/dispase (STEM CELL Technologies, CA) for 2 h at 37°C along with agitation. And then cells were filtered through a 70-μm strainer, washed twice with PBS and suspended in complete medium supplemented with insulin (Sigma-Aldrich, St. Louis, MO, USA) and epidermal growth factor (Invitrogen, USA). Cells were cultured at 37°C in a humidified atmosphere containing 95% air and 5% CO_2.

Plasmid transfection

Full-length cDNAs of the PIK3CA-WT and PIK-3CA-R88Q sequences were generated and cloned into the pCMV2-Tag2A vector following the manufacturer's instructions. ACC-83 cells

containing the PIK3CA-WT and PIK3CA-R88Q mutation constructs were all selected in DMEM with 600 mg/mL geneticin (G418) to generate stable clones.

Cell viability assay

Cell viability was assessed by a Cell Counting Kit-8 (CCK-8) assay (Bimake, Houston, USA). After cells seeded in 96-well plates at a density of 2,000 cells for each well, serial dilutions of the PI3K inhibitor or vehicle (the same volume of DMSO) were added for 72 h. The IC50 values were calculated through GraphPad Prism software 7.0.

Statistical analyses

Analyses were performed by GraphPad Prism version 7.0 (GraphPad Software, La Jolla, CA, USA). The analyses results are presented as mean ± SEM, which were at least triplicate samples per group. Data of this study was performed by one-way ANOVA to evaluate differences of groups. P<0.05 was considered statistically significant.

Results

Patient cohort, clinical information, and mutational profile of ACC

34 patients were enrolled in our study; 19 were female and 15 were male. 5 patients (14.7%) had recurrent tumors, and the others had primary tumors. As shown in Table S1, 9 tumors exhibited varying proportion of solid components, accounting more than 30% of the tumor; the other tumors (n = 25) exhibited a mixed tubular and cribriform arrangement of tumor cells.

To determine the genomic alterations in this group, patients with ACC, we performed WES to describe the landscape of somatic genetic alterations of the 34 patients with salivary ACC in this study. The average sequencing depth was 292.59× for tumors and 165.49× for normal tissues. We mapped the sequence reads to the human reference genome GRCh37/hg19 and identified a total of 873 nonsynonymous somatic mutations, including single nucleotide variations (SNVs) and insertions and deletions (In/Dels), involving in a total of 753 genes among the 34 ACC tumors. Most of the filtered and validated somatic mutations were mainly

missense mutations. A median of 25 mutations was present in each tumor (range 11-54), accordingly an average of 0.93 mutations/Mb, which was lower than that in other solid tumors in head and neck (**Figure 1A**). Mutational signature analysis of 96 substitution patterns identified 3 signatures in the ACC samples (signatures A, B and C; in Figure S1). Signature C was featured by C>T mutations and was similar to the previously described Signature6 (correlation similarity: 0.82), which is associated with defective DNA mismatch repair. The cosine correlation similarity between signatures A and B and the previously described signatures was low (cosine similarity = 0.76 and 0.51 respectively).

The overall genetic alterations in our study mostly coincide with previous reported in The Cancer Genome Atlas (TCGA, adenoid Cystic Carcinoma Project, 2019). We identified several altered genes that were markedly enriched in chromatin remodeling, Notch signaling pathway and PI3K signaling, for example, NOTCH1, NOTCH2, ARID1A, KMT2C, KDM6A and KMT2D. In addition to MYB/MYBL1-NFIB fusion gene (58.82%), we also found other alterations in MYB and NFIB in several tumors, including amplification and missense mutation. Other high frequently mutated genes ANAPC1 (17.68%), ANKRD18B (14.71%), GYPB (11.76%), MYPOP (8.82%), RUNX1 (8.82%) and RPL5 (8.82%) regulate the proliferation or apoptosis of tumor cells by participating in different cellular biological processes. In addition, MDM4 and MDM2, regulators of P53 in the DNA damage response, were amplified in several solid tumor (**Figure 1C**).

WES data was also applied to depict the somatic copy number variations (CNV) in ACC. The most common CNVs were amplifications of 1q21.1 (NOTCH2), 19p13.2 (MUC16), and 4q24 (FAT4, FBXW7) (q<0.01) and losses of 12q13.13, and 6q26 (q<0.01).

The somatic mutations, CNVs, and fusion transcripts according to the ACC pathological subtype are illustrated in **Figure 1**. We analyzed the somatic mutation frequency profiles across the genome. At the genome-wide level, MYB (67%), ARID1A (67%), NOTCH2 (78%), SMARCA2 (56%), MDM4 (67%), KMT2C (67%), HRAS (44%), and EP300 (44%) were more significantly altered in solid ACC than in other types of ACC. Other genes, including NFIB, RPL5,
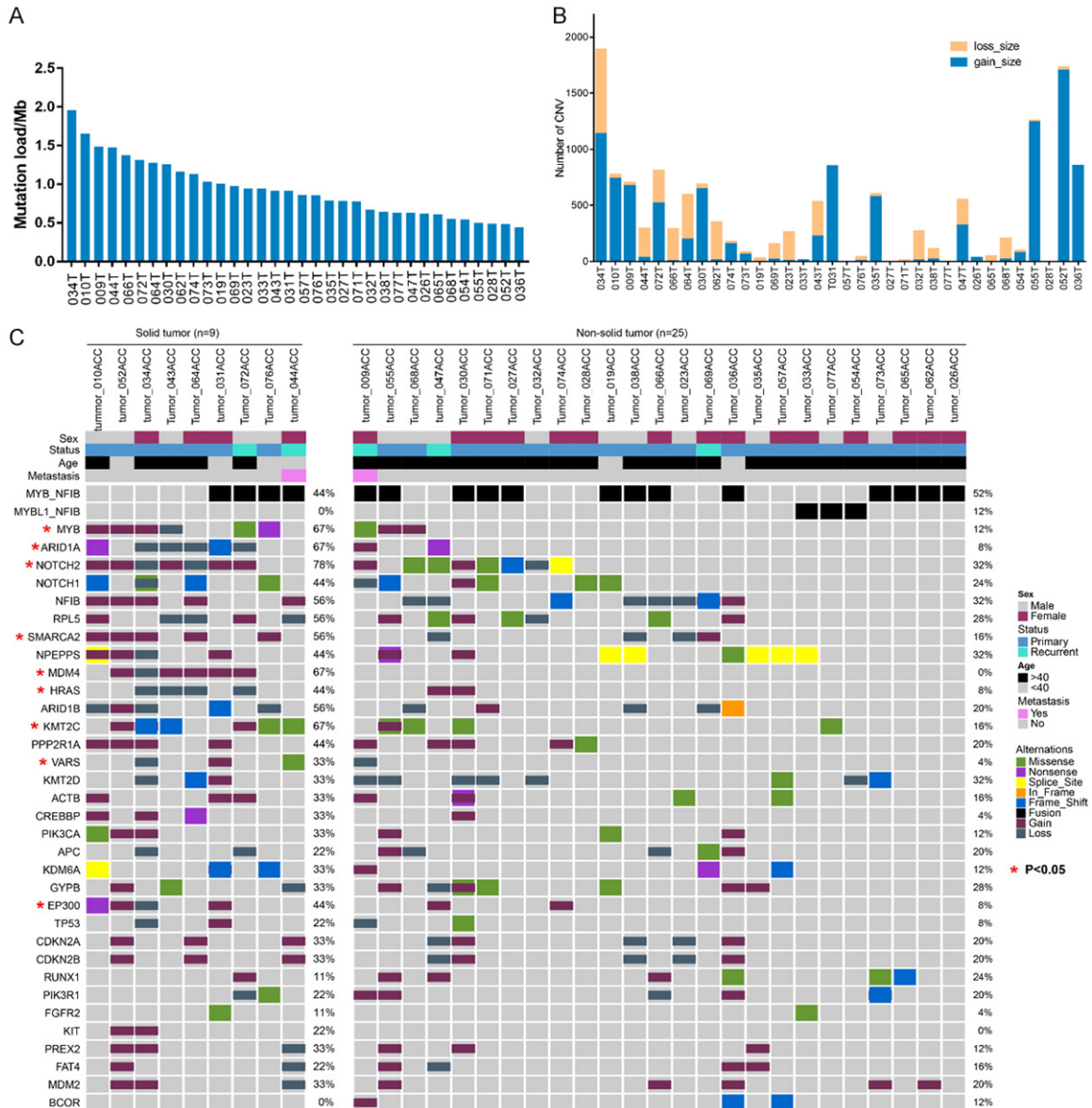
Figure 1. The genomic profiles of solid ACC and non-solid ACC. A, B. Mutation burden and CNVs of ACC. C. The landscape of solid and non-solid ACC. The left column exhibits high-frequency gene alterations in solid ACC; the right column, non-solid ACC. The percentages of samples harboring the mutant genes with respect to the total number of samples are listed on the right sides of the two columns. The different colors represented different types of gene alterations. The red asterisk indicates the genes with significant differences (P<0.05).

ARID1B, and NPEPPS, were observed to have a high mutation frequency across all types ACC.

Establishment of ACC PDXs and clinical information of the patients

Tumor specimen were obtained from 34 ACC patients and implanted subcutaneously in the nude mice after simple processing procedure (n≥3). A total of 13 PDX models successfully grew through at least 3 serial passages, corresponding to a take rate of 38%, which was

lower than that of other solid tumors [27]. According to the demographic characteristics, 6 of these tumor specimens were obtained from male patients and 7 were obtained from female (**Table 1**). At the time of surgery, these patients were 26-70 years old (median, 55 years old). 6 tumors were present in major salivary glands, 2 in the minor salivary glands in the palate and the base of the tongue, 3 in the maxillary sinus and 2 in the maxilla. Of these 13 PDXs, 2 were derived from recurrent tumors

Table 1. The successfully engrafted PDXs and their matched patients' information

No.	Age	Sex	Status	Site	Pathological type	FISH* of patient tumors	RNA-Seq of patient tumors	Time to 1st PDX (Days)	Last passage	FISH* of PDXs	RNA-seq of PDXs	Pathological type of PDXs	Matched normal tissue
009	70	Female	Recurrent tumor	submandibular gland	Cribriform/Tubular	+	MYB-NFIB	126	P6	+	MYB-NFIB	Cribriform/Tubular	P[a]
010	52	Male	Primary tumor	maxillary bone Zygomatic bone	Cribriform/Tubular/Solid (Solid 50%)	-	-	96	P7	-	-	Solid	P
019	30	Male	Primary tumor	Palate	Cribriform/Tubular/Solid (Solid 20%)	+	MYB-NFIB	219	P6	+	MYB-NFIB	Cribriform/Tubular	F[b]
023	66	Male	Primary tumor	sublingual gland	Cribriform/Tubular	ND**	-	96	P3	-	-	Cribriform/Tubular	F
026	58	Female	Primary tumor	sublingual gland	Cribriform/Tubular	+	MYB-NFIB	150	P4	+	MYB-NFIB	Cribriform/Tubular	F
031	38	Female	Primary tumor	maxillary sinus	Cribriform/Tubular/Solid (Solid 40%)	+	MYB-NFIB	87	P4	+	MYB-NFIB	solid	P
033	61	Female	Primary tumor	submandibular gland	Cribriform/Tubular	-	MYBL1-NFIB	164	P2	-	MYBL1-NFIB	Cribriform/Tubular	F
034	62	Female	Primary tumor	maxillary sinus	Cribriform/Tubular/Solid (Solid 80%)	+	NFIB-MAP3K5	76	P6	+	NFIB-MAP3K5	Solid	N
044	26	Female	Recurrent tumor	maxillary sinus	Cribriform/Tubular/Solid (Solid 80%)	+	MYB-NFIB	32	P6	+	MYB-NFIB	Solid	F
047	55	Male	Recurrent tumor	submandibular gland	Cribriform/Tubular	-	-	126	P2	-	-	Cribriform/Tubular	F
052	33	Male	Primary tumor	maxillary bone	Cribriform/Tubular/Solid (Solid 50%)	-	-	102	P2	ND	-	Solid	F
055	55	Male	Primary tumor	Base of Tongue	Cribriform/Tubular (Solid 10%)	+	MYB-NFIB	98	P2	+	MYB-NFIB	Cribriform/Tubular	F
057	67	Female	Primary tumor	Parotid gland	Cribriform/Tubular	-	-	62	P3	-	-	Cribriform/Tubular	F

*MYB break apart probe; **ND, not done. a, paraffin-embedded tissue; b, frozen tissue.

and the rest derived from primary untreated tumors (**Table 1**).

The preliminary engrafted tumors were quite indolent and required 113.21±45.84 days to attain the standard volume (600-800 mm³). The tumor growth latency period was decreased in subsequent serial passages (mean engraftment time in passage 3 to reach 600 mm³: approximately 72.5±4.95 days; to reach 1000 mm³: 102.5±2.25 days) tumor growth (Figure S2).

PDXs conserved the original histomorphological and molecular features through passaging

Among the 13 engrafted PDXs, 6 were cribriform or tubular type and 7 were mixed-type with different percentages of solid components (ranging from 10%-80%). Especially for patient tumors with solid components more than 30% (5 cases), the corresponding PDX tumors were composed completely of solid components after several passage engraftments. Immunohistochemical staining of the epithelial marker CK19, myoepithelial marker p63, tumor proliferation marker Ki67 and ACC specific marker MYB was performed on the patient tumors and PDX, respectively (**Figure 2A**). The histological morphology and immunohistochemical biomarkers in the original patient tumors were mainly preserved in the PDXs. As shown in **Figure 2**, histologic comparison of PDXs with the matched tumors showed no obvious differences in tumor morphology; tubular, cribriform and solid arrangements of tumor cells were preserved. Moreover, MYB fusion was also found across the implanted PDXs. As summarized in **Table 1**, MYB-NFIB fusion was identified in 7 tumors and was also verified through RNA-seq and RT-PCR (Figure S3). Here, a dual color break apart probe targeting MYB was applied for detection of this fusion in patient tumors and PDXs. A signal pattern consisting of one separate red or green signal indicates one normal 6q23.3-q23.3 locus and the other affected by a translocation. The FISH analysis of two patient tumors and their matched PDXs (019-ACC and 044-ACC) were shown in **Figure 2**; both of these tumors were positive for the MYB break apart signal (**Figure 2A**).

Somatic mutations is maintained in ACC PDXs

To assess whether the ACC molecular subtypes were preserved in the matched PDXs, we per-

formed genomic analysis to systematically compare the two groups. WES resulted in 223× coverage more than 99.75% of the target exome in PDXs, 243× coverage over 99.77% of the target exome in tumors, and 137× coverage more than an average of 99.62% of the exome in normal samples (PBMCs or normal salivary gland tissues).

Firstly, germline genomic DNA extracted from normal salivary gland tissues or PBMCs of each patient was used as the reference genome. Tumor mutation burden (TMB) of PDXs remained as low as those in the patient tumors (TMB in PDXs: 1.035 mutations/Mb; TMB in patients: 1.037 mutations/Mb), but no significant differences were observed between the two groups (P = 0.73), which indicating the consistency between the PDXs and their matched tumors (**Figures 2C**, S4). The C>T transition was ubiquitous in all the 13 ACC PDXs.

Next, parallel exome sequencing analyses of the PDXs and matched tumors were performed. A high correlation was found between PDXs and tumors in the total number of somatic non-synonymous SNVs and In/Dels (**Figure 2B**). The detected mutations and copy numbers were highly conserved in the PDXs. Pearson correlation analysis of the changes of SNVs and In/Dels in the PDXs and matched patients tumors showed that the correlation coefficient (R^2) was between 0.958 and 0.982, suggesting a strong correlation between the two groups (**Figure 2B**). Then, the Wilcoxon signed-rank test was performed on CNVs in the PDXs and patient tumors, and no significant difference was found (P = 0.33). Moreover, Genomic Identification of Significant Targets in Cancer (GISTIC) mainly identifies the recurrent amplification or deletion of fragments in the genome throughout the sample population. Each mutated segment is given a G-score, and the overall amplification or deletion trend is finally obtained. Here, the G-score was obtained by analyzing the PDXs and patient tumors, and the two groups were found to correspond to each other (Figure S4). In **Figure 2**, it showed the profiles of the most frequently mutated genes, somatic CNVs, and fusion transcripts were provided by clinical molecular subtype. We analyzed the somatic mutation frequency profiles across genes using the program MuSic. Despite the low overall mutation frequency, 394 mutations were identified across 342 mutated genes in patient
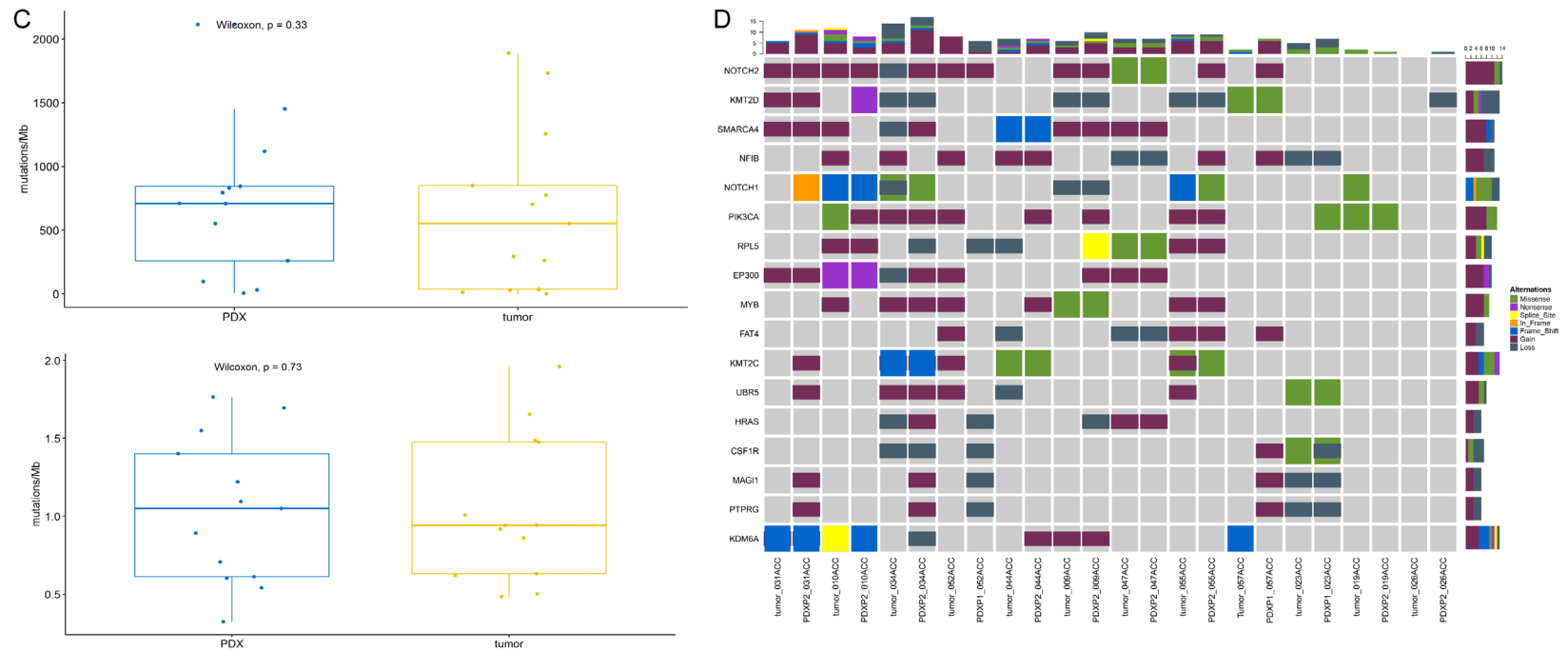
Figure 2. Genetic consistency between the patient tumors and matched PDXs. A. Histological analysis of ACC patient tumors and PDXs. HE and IHC staining of human ACC tumors. The image in the box denoted with dotted black lines in the first panel is magnified in the second panel. The tumors from patients 019-ACC and 044-ACC and their matched PDXs were hybridized with the MYB break-apart probe. Both groups showed a positive pattern-one separate green signal and one red signal as indicated by the white arrows in the third panel. Scale bars: 500 μm (first panel); 250 μm (middle three panels); and 100 μm (fifth panel). B. Correlation matrix showing the Pearson correlation coefficient between each tumor and PDX (R^2: 0.958-0.984). C. The Wilcoxon signed-rank test was used to compare the correlations of SNVs and CNV between case-matched PDXs (P>0.05). D. The frequencies of significantly altered genes, including mutations, gains and losses, in patient tumors versus PDXs are shown.

tumors, and 185 (54.09%) of these were present in both the patient tumors and PDXs across 13 tumors. And then we assessed our PDXs for the maintenance of variants described previously, which were significantly mutated in the TCGA cohort of ACC. Genes with reported mutations in the cohort included NOTCH2 (53.85%), PIK3CA (46.15%), KMT2D (46.15%), KDM6A (42.13%), KMT2C (42.31%), SMARCA4 (42.31%), and NOTCH1 (42.31%). High-frequency mutations were also detected in EP300, NFIB, RPL5, and so on. Almost putative driver mutations were conserved in the matched PDXs, as shown in **Figure 2D**.

CNVs are conserved when passaging

The Copy number variations were estimated by comparing the tumor or PDX data with data from normal samples. To evaluate whether CNVs were conserved, we assessed the correlation coefficient between paired tumors and PDXs. The Pearson correlation coefficient between the tumors and corresponding PDXs ranged from 0.958 to 0.982 and was significantly higher. Recurrent CNVs included amplifications and losses in chromosomes 2q11.1, 4q35.2, 2q11.2 and 4p16.3. In addition, we evaluated genes known to exhibit CNVs. We detected amplifications of NOTCH2, SMARCA4, PIK3CA, EP300, and MYB and loss of KMT2D in patient tumors and the corresponding PDXs (**Figure 2D**).

New fusion genes identified in our cohort and PDXs

As summarized in **Table 1**, we identified the previously reported fusion gene MYB-NFIB in 7 PDXs, and this fusion was also detected in their matched PDXs. Another fusion gene, NFIB-MAP3K5, observed in a patient tumor (034-ACC) was conserved in subsequent engrafted mice, and was verified by RT-PCR and Sanger sequencing (Figure S3).

In vivo evaluation of RA efficacy

To validate drug efficacies, we proceeded an evaluation according to our genetically and histologically characterized ACC PDX models. First, single-agent treatment with RA (40 mg/kg) and cisplatin (5 mg/kg) were performed in the PDX models (044-PDX, **Figure 3**). Treatment of this PDX model, which harbored the MYB-

NFIB fusion gene and PIK3CA amplification, resulted in varying degrees of TGI. RA (TGI = 61.83%) exhibited a better tumor growth inhibitory effect than cisplatin (TGI = 46.55%), although the difference between the RA-treated group and the combination group (TGI = 63.22%) was not obvious. In addition, the toxicities of RA and cisplatin were with well tolerance during the treatment period. To confirm that the TGI induced by RA was specific to downregulation of MYB, we performed IHC staining of MYB in the PDXs after treatment in 28 days. Treatment of 044-PDX with RA with/without cisplatin inhibited MYB expression to various degrees. However, cell proliferation, as assessed by Ki67 staining, was reduced significantly in all treatment groups. Statistical analysis of the MYB and Ki67 staining results showed no difference between the groups treated with RA with or without cisplatin.

In vivo effects of alpelisib combined with cisplatin in a PDX with PIK3CA amplification

According to the WES results, 044-PDX harbored both MYB-NFIB fusion and PIK3CA amplification; hence, we tested the antitumor effect of alpelisib combined with cisplatin in 044-PDX. In this PDX model, the combination of alpelisib and cisplatin showed greater inhibition of tumor growth (TGI = 68.88%) than did single-agent treatment. The inhibitory effects of single-agent treatment with alpelisib (54.44%) and cisplatin (46.50%) did not differ significantly (**Figure 4A**, **4B**). Additionally, the toxicities of alpelisib and cisplatin were well tolerated during the treatment period.

We detected the protein levels of P110α, AKT, ERK and the phosphorylation levels of AKT and ERK after 28 days of treatment (**Figure 4C**). The combination treatment (alpelisib and cisplatin) caused significant reductions in the level of P110α, MYB, p-AKT and p-ERK. Alpelisib treatment either with or without cisplatin inhibited P110α expression. Interestingly, the MYB level was also decreased after alpelisib treatment. In addition, we performed IHC staining of MYB and Ki67 in all treatment groups. The combination treatment resulted in a marked reduction in both the number of Ki67-labeled cells and the MYB level. However, no significant difference was observed between the alpelisib and cisplatin treated groups (**Figure**
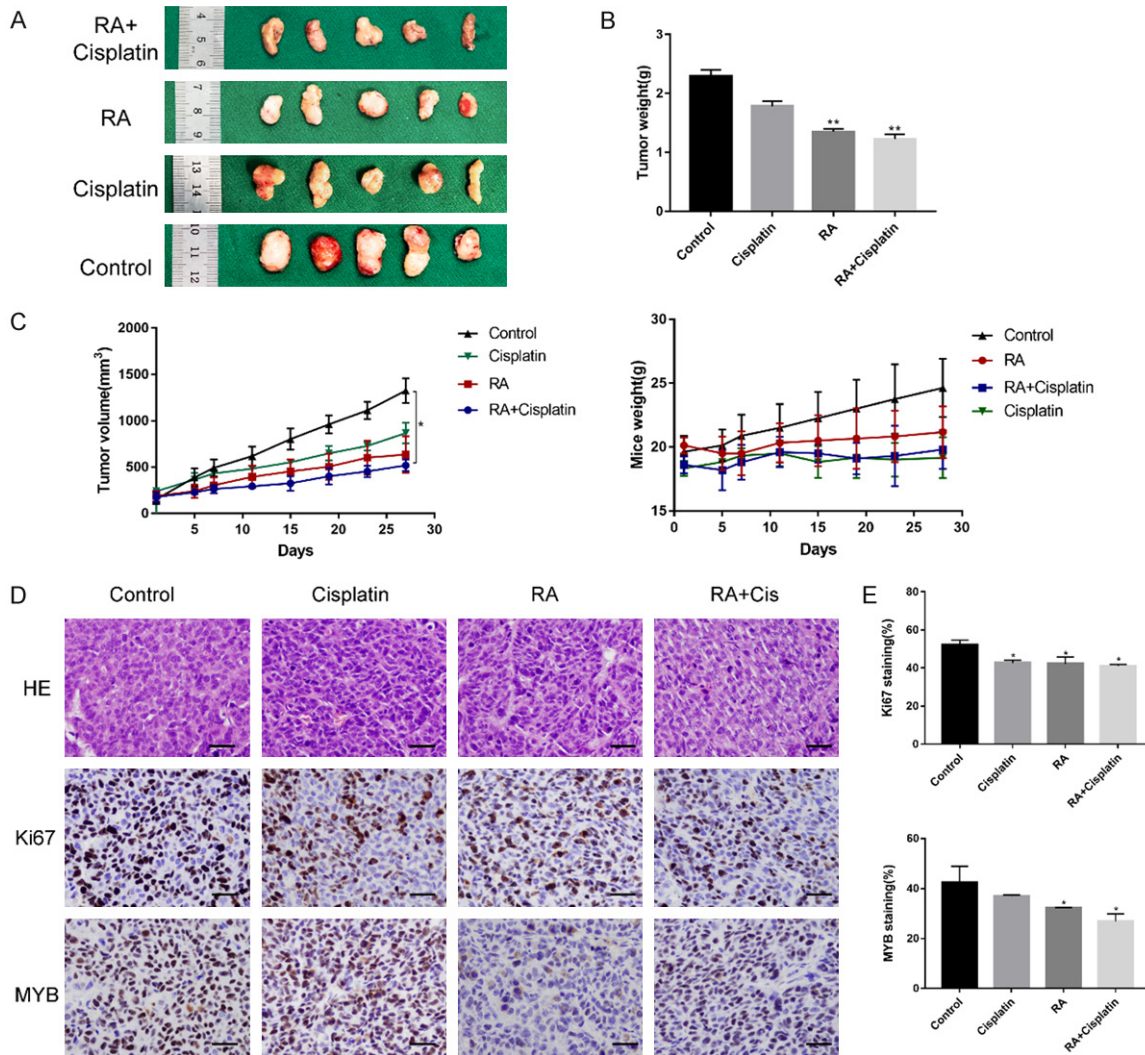
Figure 3. In vivo drug efficacy evaluation in MYB-NFIB-positive PDX models. A-C. Retinoic acid and cisplatin were administered orally to mice bearing PDX models (044-PDX, the third passage, P3) daily for 28 days. Tumor volumes and mouse weights were measured twice weekly, and the results are summarized as the mean ± SD values (Student's t-test), n = 5. D, E. HE and immunohistological staining of MYB and Ki67 in tumors were performed on samples from the four groups after 28 days of treatment. The MYB and Ki67 staining scores are summarized as the mean ± SD values, *P<0.05, **P<0.01. Scale bar: 250 μm.

4E, **4F**). Furthermore, we evaluated the inhibitory efficacy of alpelisib in combination with cisplatin in patient-derived orthotopic xenografts. However, alpelisib did not exert inhibitory effect on lung metastasis (data not shown).

In vivo effects of alpelisib combined with RA in a PDX with the PIK3CA^{R88Q} mutation

We also evaluated the inhibitory effects of alpelisib and RA in 019-PDX, which harbored PIK3CA^{R88Q} mutation and MYB-NFIB fusion. The combination of alpelisib and RA induced stronger inhibition of tumor growth than either agent

alone (TGI = 67.84%, **Figure 5E**). Combination treatment with alpelisib and RA resulted in marked reductions in both the number of Ki67-labeled cells and the MYB level (**Figure 5E**, **5F**).

Effects of alpelisib on proliferation and PI3K pathway activity in ACC cells harboring PIK3CA alterations

To evaluate the oncogenic potential of amplified or mutant forms of PIK3CA, we stably transfected ACC-83 cells with plasmids containing the wild-type (wt) or R88Q mutant P110α subunit of PI3K or empty vector. As
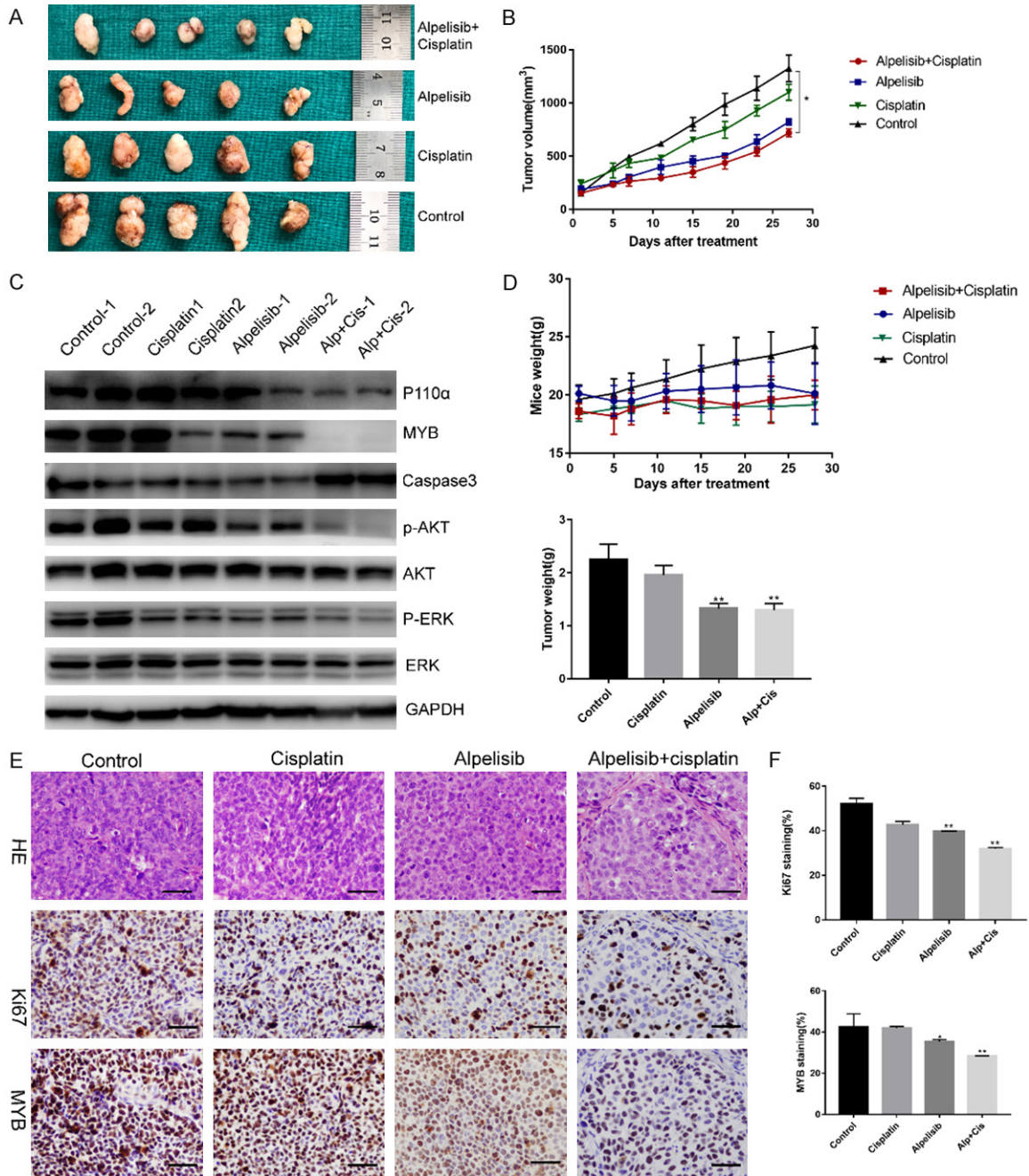
Figure 4. In vivo drug efficacy evaluation in PDX models with PIK3CA amplification. A-D. Alpelisib (25 mg/kg) and cisplatin (5 mg/kg) were administered to PDX-bearing mice (044-PDX, the third passage, P3) daily for 28 days. Tumor volumes, tumor weights and mouse weights were monitored and measured, and the results were summarized as the mean ± SD. n = 5, *P<0.05, **P<0.01. Immunoblot analysis of MYB, Caspase3 and PI3K signaling pathway components in tumors after 28 days of treatment. E. Representative images of HE, Ki67 and MYB staining in tumors after 28 days of treatment with alpelisib and cisplatin. F. The Ki67 and MYB staining scores are summarized as the mean ± SEM values. Scale bar: 250 μm.

shown in **Figure 6**, cells transfected with the wt or mutant PIK3CA plasmid showed comparable increases in the level of p110α. As a consequence of PI3K activation, the phosphoryla-

tion of AKT at both Ser473 and Thr308 as well as p-S6 were increased. The effects of the PI3K inhibitor alpelisib on cell proliferation were evaluated by a CCK-8 assay. Alpelisib
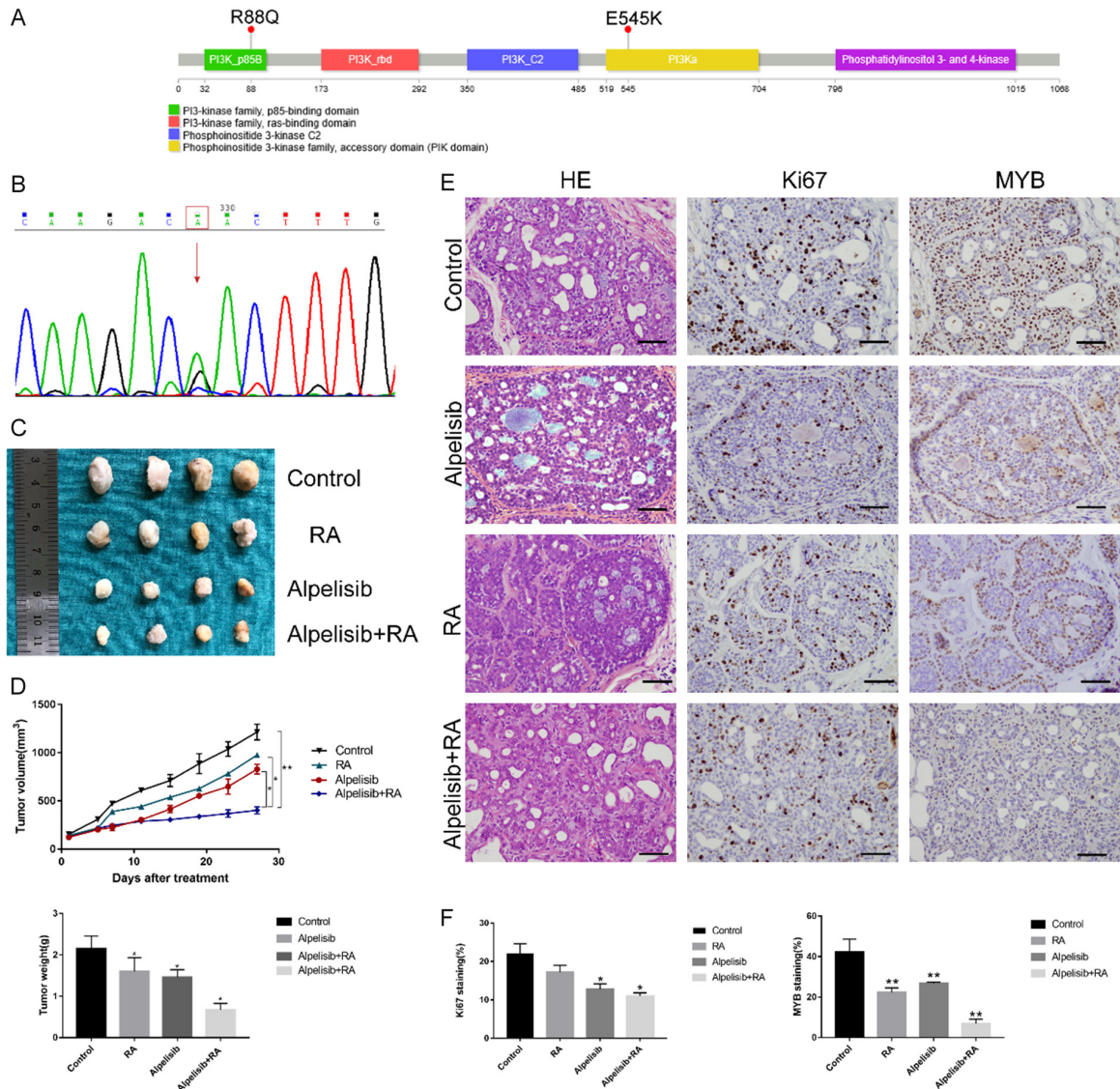
Figure 5. In vivo drug efficacy evaluation in PDX models with PIK3CA mutation and the MYB-NFIB fusion. A. Schematic illustration of PIK3CA mutations. B. The PIK3CA mutation status of 019-ACC and the corresponding PDX are shown. C-F. A PDX harboring PIK3CA^{R88Q} (019-PDX, the third passage, P3) was treated with alpelisib and a combination of alpelisib and RA, n = 4. Tumor volumes and mouse weights were measured twice daily. HE and IHC staining results are shown. Scale bar: 250 μm. *P<0.05, **P<0.01.

impaired cell proliferation in a concentration-dependent manner in both PIK3CA-amplified and PIK3CA-mutated cells. The concentration required to achieve the half-maximal inhibition of cell proliferation was approximately 3.583 to 8.299 μmol/L in cells with PIK3CA-amplification and 1.354 to 3.353 μmol/L in cells with PIK3CA mutation. Then we analyzed the modulation of PI3K-AKT pathway activity in transfected cells with PIK3CA amplification/mutation. Alpelisib inhibited the phosphoryla-

tion of AKT (Ser473 and Thr308) and p-S6 independent of the PIK3CA status (**Figure 6**).

Next, we tried to isolate patient-derived xenograft cells (PDCs) from the established PIK3CA-amplified PDX (044-PDX) for in vitro assays. The morphological characteristics of the PDCs were shown in **Figure 6A**. In PDCs with PIK3CA amplification, alpelisib (0.1 and 1 nM) dose-dependently inhibited P110α level and PI3K/AKT signaling after treatment at 2, 4 and 6
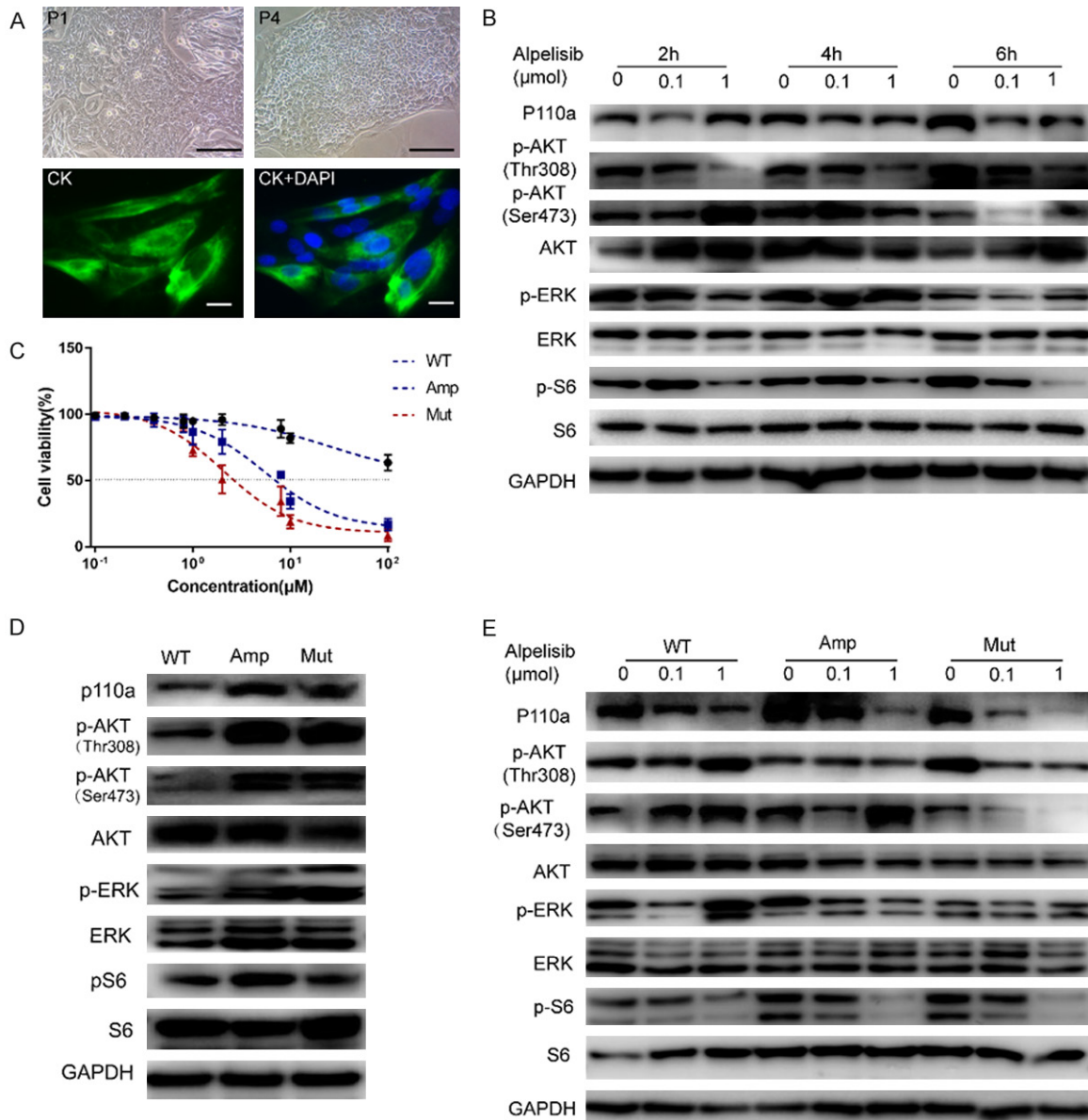
Figure 6. In vitro drug efficacy evaluation using PIK3CA^WT and PIK3CA^R88Q cells. A. Morphology of ACC cell cultures and expression of the epithelial cell marker pan cytokeratin (CK) in the cells from 044-ACC PDX (the third passage, P3). First panel: 20×, scale bar, 200 μm; Second panel: 40×, scale bar, 10 μm. B. Primary cells were treated with 0.1 μmol/L and 1 μmol/L alpelisib for 2, 4, and 6 h. Cells were lysed, and the indicated protein levels were quantified by western blot analysis. C. Dose-response curves of alpelisib in 72-hour proliferation assays for ACC-83 cells transfected with cDNA of PIK3CA^WT and PIK3CA^R88Q cells. D. Western blot showing the levels of PI3K subunit P110α, pAKT (Ser473, Thr308) and pS6 in whole-cell lysates from PIK3CA^WT and PIK3CA^R88Q cells. E. Immunoblot analysis of PI3K/AKT pathway components in PIK3CA^WT and PIK3CA^R88Q cells treated with alpelisib for 6 h.

hours, as shown by the western blot results (**Figure 6**).

Discussion

The main purpose of this study was to better characterize salivary ACC, especial solid-type, though comprehensive molecular and pathological analysis. Currently, research on the key molecular drivers responsible for ACC initiation and progression has been restrained because the lack of experimental models, which hindered progress in the discovery of therapies for ACC. Therefore, the establishment of PDX models will extremely contribute to the identification of crutial genomic alterations in engrafted tumors [19]. The models are of great value and significance for exploring the processes that

lead to late recurrence and metastasis and developing novel targeted therapies [28, 29]. Compared with cell lines and other animal models, PDXs have been advocated as superior preclinical cancer models for biomarker studies and evaluation of new treatment modalities [30-32].

Over a 3-year period, we collected 34 paired tumors and normal samples from Chinese ACC patients who only underwent surgical excision without radiotherapy or chemotherapy. From these 34 ACC patients, we established 13 PDXs and successfully passaged for at least three generations, with a higher success rate (38.24%) than before. The time required for initial PDX engraftments (first passage) from patient tumors was much longer than the engraftment time for other solid tumors in head and neck [33]. Previous studies have shown that it is extremely difficult to establish ACC PDX models which requires longer periods and higher costs than that for other tumors [34, 35]. To investigate potential factors influencing PDX establishment, we evaluated the characteristics of both the patients and PDXs. We did not observe any statistically significant correlation between the PDXs and patient characteristics, such as age or sex. Regarding the pathologic features of the tumors, although the tumor site did not correlate with engraftment success, tumor histomorphology turned was relevant. In our study, 9 of the 34 ACC samples had solid components, and the rest were cribriform/tubular mixed type. 5 of the engrafted PDXs were solid-type (5 of 9, 55.56%) and the others were mixed type (8 of 25, 32%). Given the more aggressive features, solid-type ACC is more easily to survive in mice, thus the successful rate of solid-type ACC PDX is relatively higher.

The PDX group in our study was composed exclusively of patients with salivary ACC, thus capturing the clinical gene expression and mutational profiles of this disease. By comparing the genomic landscape of the PDXs to the patient tumors, we successfully confirmed that the PDXs maintained the genetic characteristics of the matched patient tumors. Known recurrently mutated genes, such as NOTCH1, KMT2C and KDM6A, and CNVs on chromosomes 2q11.1, 4q35.2, 2q11.2 and 4p16.3 were recurrently present in our patient tumors

and confirmed in the corresponding PDXs. We further performed mRNA analysis to better understand the genetic alterations. Notably, the results confirmed that MYB-NFIB fusion appeared in over 60% of the tumors, and additional fusion gene involving NFIB with a different partner (MAP3K5) was also detected. Translocated enhancers from MYB chromosomal rearrangements in ACC produce positive feedback loops that result in MYB overexpression and tumor transformation [36]. The etiologic and functional implications of the novel fusion gene need further to be explained. Potential driver events, including MYB-NFIB gene fusion, hotspot mutations of known oncogenes and inactivation of tumor suppressor genes, were also conserved in the corresponding PDXs. The PDXs partly recapitulated the molecular and genetic characteristics of the original patient tumors.

Although the sample size in this study was small, the pathological type classifier in our study was related to the xenograft growth rate. In our sequenced cohort, genomic alterations were captured and this study showed how effectively ACC PDXs could individually maintain their matched tumors. Recapitulation of somatic mutations, CNVs and other genomic alterations in PDXs were also described in this study, which mean the potential utility of our PDXs for exploring the mechanisms of targeted drugs in precision oncology in future.

The association between PDX engraftment success rate and poor patient prognosis has previously been discussed in other cancers, including breast cancer and squamous cell carcinoma, suggesting that engraftment ability is related to cancer aggressiveness and patient prognosis [33, 37]. When tumor tissues were implanted into immunodeficient mice, the growth rate of tumors from different patients was variable. Mice were monitored for at least 6 months, and engraftment and non-engraftment were then assessed through tumor volume. Some patient tumors grew rapidly after implantation into the mice, and the PDXs attained the standard volume for 3-4 months of growth and could be passaged continuously for at least 3 passages. After being removed from humans and transplanted into mice months later, some tumors showed signs of stagnant growth or even an inability to develop

into tumors. Of the 13 engrafted tumors found in this study, 11 exhibited nerve or bone invasion characteristics. Although PDX engraftment success was independently associated with patient prognosis, we also tried to confirm whether successful engraftment was related with any potential mutations or CNVs. The integrated frequency of genetic alterations in our PDXs and patient tumors was mainly coincident with previous TCGA findings. Molecular profiles of engrafted versus non-engrafted samples showed that the frequency in gene mutations of ARID1A, PIK3CA, EP300, and VARS was higher in the engrafted samples, which suggested that these genes might contribute to the engraftment ability.

Here, we used several established ACC PDX models to evaluate the efficiency of combination therapy targeting MYB and PIK3CA alteration. One PDX was generated from an ACC located in a minor salivary gland from the maxillary sinus that exhibited a solid histological type and generated lung metastasis in late stage. This PDX exhibited an aggressive growth pattern, growing to 1500-2000 mm^3 within 30 days. Moreover, this PDX harbored both MYB-NFIB fusion and PIK3CA amplification; thus, it was considered suitable for therapeutic development studies.

The findings of our mechanistic studies of retinoic acid receptor signaling, which inactivated MYB proteins, were consistent with those previous studies [8]. RA treatment in ACC xenografts resulted in TGI and decreased MYB expression [8]. MYB has key roles in the pathogenesis of ACC [38, 39]. In our research, in a PDX harboring the MYB-NFIB fusion gene (044-PDX), RA treatment partially inhibited tumor growth, but no significant difference was seen when RA was combined with a routine-chemotherapy.

Genomic characterization studies displayed that several genetic alterations were frequently found in PDX. Aberrant activation of PI3K signaling pathway showed a prominent role in the pathogenesis of solid tumors [40]. Previous study showed that PIK3CA altered in 5% ACC patients and mutations and amplifications of PIK3CA were frequently localized in exon 9 (E545K and E542K) and exon 20 (H1047R) [41-43]. To test the potential efficiency of attractive targeted agent for PIK3CA, the administration of PI3K inhibitor in combining with chemotherapeutics mediated tumor regression. Notably, the tumor inhibition caused by single inhibitor or combination of drugs was not accompanied by objective systemic toxicities, as displayed by the maintenance of weight during the experimental period.

Furthermore, both the results of *in vitro* and *in vivo* indicated that retinoic acid and PI3K inhibitor induced inhibition of MYB and P110α and decreased the level of its downstream signaling target genes. Our study demonstrated that alpelisib is a potent agent resistant to the ACCs bearing PIK3CA-amplification/mutation and emphasized how the repurposing of drugs can contribute to explore effective precision treatments for a specific proportion of ACC.

In vitro, the results of IHC staining and western blot analysis of ACC PDXs demonstrated potent, dose-dependent suppression of Ki67 and P110α expression and downstream PI3K signaling pathway activity. The results of PI3K inhibitor treatment indicated that the proliferation of tumor cells was suppressed and that both MYB and P110α were downregulated at different time points. In addition, we also evaluated the efficiency of RA in another PDX derived from a primary parotid tumor. In both of these PDXs, MYB fusion with the transcription factor NFIB was present, and MYB expression was high. The western blot results from the PDXs and low-passage ACC cells also showed that the levels of P110α and its downstream targets were reduced after treatment with PI3K inhibitor. In addition, MYB expression was inhibited in both the PI3K-treated group and the combination-treated group. Collectively, these data indicated the effect of this PI3K inhibitor on its expected targets and showed that the effects of this drug are enhanced when it is used in combination with other routine-chemotherapeutic drugs.

In summary, we presented preclinical evidence for the therapeutic potential of a PI3K inhibitor and RA in ACC PDXs harboring both PIK3CA-amplification/mutation and MYB-NFIB fusion. The combination of a PI3K inhibitor with RA and chemotherapeutic drugs may provide an effective, selective therapeutic approach for these ACC patients.

Disclosure of conflict of interest

None.

Address correspondence to: Jiang Li, Department of Oral Pathology, Shanghai Ninth People's Hospital, College of Stomatology, Shanghai Jiao Tong University School of Medicine, Number 639, Zhi-Zao-Ju Road, Shanghai 200011, P. R. China. Tel: +86-21-53315687; E-mail: lijiang182000@126.com; Shuyang Sun, Department of Oral and Maxillofacial-Head & Neck Oncology, Shanghai Ninth People's Hospital, College of Stomatology, Shanghai Jiao Tong University School of Medicine, Number 639, Zhi-Zao-Ju Road, Shanghai 200011, P. R. China. Tel: +86-13651629869; E-mail: shuyangs@shsmu.edu.cn

References

[1] Ali S, Palmer FL, Katabi N, Lee N, Shah JP, Patel SG and Ganly I. Long-term local control rates of patients with adenoid cystic carcinoma of the head and neck managed by surgery and postoperative radiation. Laryngoscope 2017; 127: 2265-2269.

[2] Tian Z, Li L, Zhang CY, Gu T and Li J. Differences in MYB expression and gene abnormalities further confirm that salivary cribriform basal cell tumors and adenoid cystic carcinoma are two distinct tumor entities. J Oral Pathol Med 2016; 45: 698-703.

[3] Massé J, Truntzer C, Boidot R, Khalifa E, Pérot G, Velasco V, Mayeur L, Billerey-Larmonier C, Blanchard L, Charitansky H, Soubeyran I, Iggo R, Arnould L and MacGrogan G. Solid-type adenoid cystic carcinoma of the breast, a distinct molecular entity enriched in NOTCH and CREBBP mutations. Mod Pathol 2019; 33: 1041-1055.

[4] Xu B, Drill E, Ho A, Ho A, Dunn L, Prieto-Granada CN, Chan T, Ganly I, Ghossein R and Katabi N. Predictors of outcome in adenoid cystic carcinoma of salivary glands: a clinicopathologic study with correlation between MYB fusion and protein expression. Am J Surg Pathol 2017; 41: 1422-1432.

[5] Gonda TJ and Ramsay RG. Adenoid cystic carcinoma can be driven by MYB or MYBL1 rearrangements: new insights into MYB and tumor biology. Cancer Discov 2016; 6: 125-127.

[6] Drier Y, Cotton MJ, Williamson KE, Gillespie SM, Ryan RJ, Kluk MJ, Carey CD, Rodig SJ, Sholl LM, Afrogheh AH, Faquin WC, Queimado L, Qi J, Wick MJ, El-Naggar AK, Bradner JE, Moskaluk CA, Aster JC, Knoechel B and Bernstein BE. An oncogenic MYB feedback loop drives alternate cell fates in adenoid cystic carcinoma. Nat Genet 2016; 48: 265-272.

[7] Brayer KJ, Frerich CA, Kang H and Ness SA. Recurrent fusions in MYB and MYBL1 define a common, transcription factor-driven oncogenic pathway in salivary gland adenoid cystic carcinoma. Cancer Discov 2016; 6: 176-187.

[8] Mandelbaum J, Shestopalov IA, Henderson RE, Chau NG, Knoechel B, Wick MJ and Zon LI. Zebrafish blastomere screen identifies retinoic acid suppression of MYB in adenoid cystic carcinoma. J Exp Med 2018; 215: 2673-2685.

[9] Alfieri S, Granata R, Bergamini C, Resteghini C, Bossi P, Licitra LF and Locati LD. Systemic therapy in metastatic salivary gland carcinomas: a pathology-driven paradigm? Oral Oncol 2017; 66: 58-63.

[10] Ross PJ, Teoh EM, A'hern RP, Rhys-Evans PH, Harrington KJ, Nutting CM and Gore ME. Epirubicin, cisplatin and protracted venous infusion 5-Fluorouracil chemotherapy for advanced salivary adenoid cystic carcinoma. Clin Oncol (R Coll Radiol) 2009; 21: 311-314.

[11] Ferrarotto R, Mitani Y, Diao L, Guijarro I, Wang J, Zweidler-McKay P, Bell D, William WN Jr, Glisson BS, Wick MJ, Kapoun AM, Patnaik A, Eckhardt G, Munster P, Faoro L, Dupont J, Lee JJ, Futreal A, El-Naggar AK and Heymach JV. Activating NOTCH1 mutations define a distinct subgroup of patients with adenoid cystic carcinoma who have poor prognosis, propensity to bone and liver metastasis, and potential responsiveness to Notch1 inhibitors. J Clin Oncol 2017; 35: 352-360.

[12] Wong SJ, Karrison T, Hayes DN, Kies MS, Cullen KJ, Tanvetyanon T, Argiris A, Takebe N, Lim D, Saba NF, Worden FP, Gilbert J, Lenz HJ, Razak AR, Roberts JD, Vokes EE and Cohen EE. Phase II trial of dasatinib for recurrent or metastatic c-KIT expressing adenoid cystic carcinoma and for nonadenoid cystic malignant salivary tumors. Ann Oncol 2016; 27: 318-323.

[13] Hitre E, Budai B, Takacsi-Nagy Z, Rubovszky G, Toth E, Remenar E, Polgar C and Lang I. Cetuximab and platinum-based chemoradio- or chemotherapy of patients with epidermal growth factor receptor expressing adenoid cystic carcinoma: a phase II trial. Br J Cancer 2013; 109: 1117-1122.

[14] Agulnik M, Cohen EW, Cohen RB, Chen EX, Vokes EE, Hotte SJ, Winquist E, Laurie S, Hayes DN, Dancey JE, Brown S, Pond GR, Lorimer I, Daneshmand M, Ho J, Tsao MS and Siu LL.

Phase II study of lapatinib in recurrent or metastatic epidermal growth factor receptor and/or erbB2 expressing adenoid cystic carcinoma and non adenoid cystic carcinoma malignant tumors of the salivary glands. J Clin Oncol 2007; 25: 3978-3984.

[15] Jakob JA, Kies MS, Glisson BS, Kupferman ME, Liu DD, Lee JJ, El-Naggar AK, Gonzalez-Angulo AM and Blumenschein GR Jr. Phase II study of gefitinib in patients with advanced salivary gland cancers. Head Neck 2015; 37: 644-649.

[16] Glisson B, Colevas AD, Haddad R, Krane J, El-Naggar A, Kies M, Costello R, Summey C, Arquette M, Langer C, Amrein PC and Posner M. HER2 expression in salivary gland carcinomas: dependence on histological subtype. Clin Cancer Res 2004; 10: 944-946.

[17] Dillon PM, Petroni GR, Horton BJ, Moskaluk CA, Fracasso PM, Douvas MG, Varhegyi N, Zaja-Milatovic S and Thomas CY. A phase II study of dovitinib in patients with recurrent or metastatic adenoid cystic carcinoma. Clin Cancer Res 2017; 23: 4138-4145.

[18] Zhang J, Peng B and Chen X. Expressions of nuclear factor kappaB, inducible nitric oxide synthase, and vascular endothelial growth factor in adenoid cystic carcinoma of salivary glands: correlations with the angiogenesis and clinical outcome. Clin Cancer Res 2005; 11: 7334-7343.

[19] Hidalgo M, Amant F, Biankin AV, Budinska E, Byrne AT, Caldas C, Clarke RB, de Jong S, Jonkers J, Maelandsmo GM, Roman-Roman S, Seoane J, Trusolino L and Villanueva A. Patient-derived xenograft models: an emerging platform for translational cancer research. Cancer Discov 2014; 4: 998-1013.

[20] Crystal AS, Shaw AT, Sequist LV, Friboulet L, Niederst MJ, Lockerman EL, Frias RL, Gainor JF, Amzallag A, Greninger P, Lee D, Kalsy A, Gomez-Caraballo M, Elamine L, Howe E, Hur W, Lifshits E, Robinson HE, Katayama R, Faber AC, Awad MM, Ramaswamy S, Mino-Kenudson M, Iafrate AJ, Benes CH and Engelman JA. Patient-derived models of acquired resistance can identify effective drug combinations for cancer. Science 2014; 346: 1480-1486.

[21] Nor F, Warner KA, Zhang Z, Acasigua GA, Pearson AT, Kerk SA, Helman JI, Sant'Ana Filho M, Wang S and Nor JE. Therapeutic inhibition of the MDM2-p53 interaction prevents recurrence of adenoid cystic carcinomas. Clin Cancer Res 2017; 23: 1036-1048.

[22] Cibulskis K, Lawrence MS, Carter SL, Sivachenko A, Jaffe D, Sougnez C, Gabriel S, Meyerson M, Lander ES and Getz G. Sensitive detection of somatic point mutations in impure and heterogeneous cancer samples. Nat Biotechnol 2013; 31: 213-219.

[23] Saunders CT, Wong WS, Swamy S, Becq J, Murray LJ and Cheetham RK. Strelka: accurate somatic small-variant calling from sequenced tumor-normal sample pairs. Bioinformatics 2012; 28: 1811-1817.

[24] Boeva V, Popova T, Bleakley K, Chiche P, Cappo J, Schleiermacher G, Janoueix-Lerosey I, Delattre O and Barillot E. Control-FREEC: a tool for assessing copy number and allelic content using next-generation sequencing data. Bioinformatics 2012; 28: 423-425.

[25] Mitani Y, Li J, Rao PH, Zhao YJ, Bell D, Lippman SM, Weber RS, Caulin C and El-Naggar AK. Comprehensive analysis of the MYB-NFIB gene fusion in salivary adenoid cystic carcinoma: incidence, variability, and clinicopathologic significance. Clin Cancer Res 2010; 16: 4722-4731.

[26] Han J, Zhang C, Gu T, Yang X, Hu L, Tian Z, Li J and Zhang C. Analysis of clinicopathological characteristics, MYB rearrangement and prognostic factors in salivary adenoid cystic carcinoma. Oncol Lett 2019; 17: 2915-2922.

[27] Rothenberg SM and Ellisen LW. The molecular pathogenesis of head and neck squamous cell carcinoma. J Clin Invest 2012; 122: 1951-1957.

[28] Crystal AS, Shaw AT, Sequist LV, Friboulet L, Niederst MJ, Lockerman EL, Frias RL, Gainor JF, Amzallag A, Greninger P, Lee D, Kalsy A, Gomez-Caraballo M, Elamine L, Howe E, Hur W, Lifshits E, Robinson HE, Katayama R, Faber AC, Awad MM, Ramaswamy S, Mino-Kenudson M, Iafrate AJ, Benes CH and Engelman JA. Patient-derived models of acquired resistance can identify effective drug combinations for cancer. Science 2014; 346: 1480-1486.

[29] Krepler C, Sproesser K, Brafford P, Beqiri M, Garman B, Xiao M, Shannan B, Watters A, Perego M, Zhang G, Vultur A, Yin X, Liu Q, Anastopoulos IN, Wubbenhorst B, Wilson MA, Xu W, Karakousis G, Feldman M, Xu X, Amaravadi R, Gangadhar TC, Elder DE, Haydu LE, Wargo JA, Davies MA, Lu Y, Mills GB, Frederick DT, Barzily-Rokni M, Flaherty KT, Hoon DS, Guarino M, Bennett JJ, Ryan RW, Petrelli NJ, Shields CL, Terai M, Sato T, Aplin AE, Roesch A, Darr D, Angus S, Kumar R, Halilovic E, Caponigro G, Jeay S, Wuerthner J, Walter A, Ocker M, Boxer MB, Schuchter L, Nathanson KL and Herlyn M. A comprehensive patient-derived xenograft collection representing the heterogeneity of melanoma. Cell Rep 2017; 21: 1953-1967.

[30] Li J, Ye C and Mansmann UR. Comparing patient-derived xenograft and computational response prediction for targeted therapy in patients of early-stage large cell lung cancer. Clin Cancer Res 2016; 22: 2167-2176.

[31] Lilja-Fischer JK, Ulhoi BP, Alsner J, Stougaard M, Thomsen MS, Busk M, Lassen P, Steiniche

T, Nielsen VE and Overgaard J. Characterization and radiosensitivity of HPV-related oropharyngeal squamous cell carcinoma patient-derived xenografts. Acta Oncol 2019; 58: 1489-1494.

[32] Lin W, Yip YL, Jia L, Deng W, Zheng H, Dai W, Ko JMY, Lo KW, Chung GTY, Yip KY, Lee SD, Kwan JS, Zhang J, Liu T, Chan JY, Kwong DL, Lee VH, Nicholls JM, Busson P, Liu X, Chiang AKS, Hui KF, Kwok H, Cheung ST, Cheung YC, Chan CK, Li B, Cheung AL, Hau PM, Zhou Y, Tsang CM, Middeldorp J, Chen H, Lung ML and Tsao SW. Establishment and characterization of new tumor xenografts and cancer cell lines from EBV-positive nasopharyngeal carcinoma. Nat Commun 2018; 9: 4663.

[33] Karamboulas C, Bruce JP, Hope AJ, Meens J, Huang SH, Erdmann N, Hyatt E, Pereira K, Goldstein DP, Weinreb I, Su J, O'Sullivan B, Tiedemann R, Liu FF, Pugh TJ, Bratman SV, Xu W and Ailles L. Patient-derived xenografts for prognostication and personalized treatment for head and neck squamous cell carcinoma. Cell Rep 2018; 25: 1318-1331, e4.

[34] Cornett A, Athwal HK, Hill E, Murphy G 3rd, Yeoh K, Moskaluk CA, Witt RL, D'Silva NJ, Agarwal S and Lombaert IMA. Serial patient-derived orthotopic xenografting of adenoid cystic carcinomas recapitulates stable expression of phenotypic alterations and innervation. EBioMedicine 2019; 41: 175-184.

[35] Keysar SB, Eagles JR, Miller B, Jackson BC, Chowdhury FN, Reisinger J, Chimed TS, Le PN, Morton JJ, Somerset HL, Varella-Garcia M, Tan AC, Song JI, Bowles DW, Reyland ME and Jimeno A. Salivary gland cancer patient-derived xenografts enable characterization of cancer stem cells and new gene events associated with tumor progression. Clin Cancer Res 2018; 24: 2935-2943.

[36] Persson M, Andren Y, Mark J, Horlings HM, Persson F and Stenman G. Recurrent fusion of MYB and NFIB transcription factor genes in carcinomas of the breast and head and neck. Proc Natl Acad Sci U S A 2009; 106: 18740-18744.

[37] Goetz MP, Kalari KR, Suman VJ, Moyer AM, Yu J, Visscher DW, Dockter TJ, Vedell PT, Sinnwell JP, Tang X, Thompson KJ, McLaughlin SA, Moreno-Aspitia A, Copland JA, Northfelt DW, Gray RJ, Hunt K, Conners A, Sicotte H, Eckel-Passow JE, Kocher JP, Ingle JN, Ellingson MS, McDonough M, Wieben ED, Weinshilboum R, Wang L and Boughey JC. Tumor sequencing and patient-derived xenografts in the neoadjuvant treatment of breast cancer. J Natl Cancer Inst 2017; 109: djw306.

[38] Ramsay RG and Gonda TJ. MYB function in normal and cancer cells. Nat Rev Cancer 2008; 8: 523-534.

[39] West RB, Kong C, Clarke N, Gilks T, Lipsick JS, Cao H, Kwok S, Montgomery KD, Varma S and Le QT. MYB expression and translocation in adenoid cystic carcinomas and other salivary gland tumors with clinicopathologic correlation. Am J Surg Pathol 2011; 35: 92-99.

[40] Sivaram N, McLaughlin PA, Han HV, Petrenko O, Jiang YP, Ballou LM, Pham K, Liu C, van der Velden AW and Lin RZ. Tumor-intrinsic PIK3CA represses tumor immunogenecity in a model of pancreatic cancer. J Clin Invest 2019; 129: 3264-3276.

[41] Ho AS, Kannan K, Roy DM, Morris LG, Ganly I, Katabi N, Ramaswami D, Walsh LA, Eng S, Huse JT, Zhang J, Dolgalev I, Huberman K, Heguy A, Viale A, Drobnjak M, Leversha MA, Rice CE, Singh B, Iyer NG, Leemans CR, Bloemena E, Ferris RL, Seethala RR, Gross BE, Liang Y, Sinha R, Peng L, Raphael BJ, Turcan S, Gong Y, Schultz N, Kim S, Chiosea S, Shah JP, Sander C, Lee W and Chan TA. The mutational landscape of adenoid cystic carcinoma. Nat Genet 2013; 45: 791-798.

[42] Ho AS, Ochoa A, Jayakumaran G, Zehir A, Valero Mayor C, Tepe J, Makarov V, Dalin MG, He J, Bailey M, Montesion M, Ross JS, Miller VA, Chan L, Ganly I, Dogan S, Katabi N, Tsipouras P, Ha P, Agrawal N, Solit DB, Futreal PA, El Naggar AK, Reis-Filho JS, Weigelt B, Ho AL, Schultz N, Chan TA and Morris LG. Genetic hallmarks of recurrent/metastatic adenoid cystic carcinoma. J Clin Invest 2019; 129: 4276-4289.

[43] Bonelli MA, Cavazzoni A, Saccani F, Alfieri RR, Quaini F, La Monica S, Galetti M, Cretella D, Caffarra C, Madeddu D, Frati C, Lagrasta CA, Falco A, Rossetti P, Fumarola C, Tiseo M, Petronini PG and Ardizzoni A. Inhibition of PI3K pathway reduces invasiveness and epithelial-to-mesenchymal transition in squamous lung cancer cell lines harboring PIK3CA gene alterations. Mol Cancer Ther 2015; 14: 1916-1927.

Table S1. Clinical information of all ACC patients in this study

Number	age	sex	status	Site	pathological type	MYB/MYBL1 break-apart	Metastasis
009ACC	70	Female	Recurrent	Submandibular gland	Cribriform/Tubular	+	lung
010ACC	52	Male	Primary	Maxillary bone Zygomatic bone	Solid	-	
019ACC	30	Male	Primary	Palate	Cribriform/Tubular	+	
023ACC	66	Male	Primary	Sublingual gland	Cribriform/Tubular	-	
026ACC	58	Female	Primary	Sublingual gland	Cribriform/Tubular	+	
027ACC	58	Female	Primary	Sublingual gland	Cribriform/Tubular	+	
028ACC	42	Female	Primary	Palate	Cribriform/Tubular	-	
030ACC	66	Female	Primary	Submandibular gland	Cribriform/Tubular	+	
031ACC	38	Female	Primary	Maxillary sinus	Cribriform/Tubular/Solid (Solid 40%)	-	
032ACC	71	Male	Primary	Sublingual gland	Cribriform/Tubular	-	
033ACC	61	Female	Primary	Submandibular gland	Cribriform/Tubular	MYBL1+	
034ACC	62	Female	Primary	Maxillary sinus	Solid	-	
035ACC	42	Male	Primary	Sublingual gland	Cribriform/Tubular	-	
036ACC	36	Female	Primary	Palate	Cribriform/Tubular	+	
038ACC	53	Male	Primary	Parotid gland	Cribriform/Tubular	+	
043ACC	56	Male	Primary	Submandibular gland	Solid	-	
044ACC	26	Female	Recurrent	Maxillary sinus	Solid	+	lung
047ACC	55	Male	Recurrent	Submandibular gland	Cribriform	-	
052ACC	33	Male	Primary	Maxillary bone	Solid	-	
054ACC	61	Female	Primary	Sublingual gland	Cribriform/Tubular	MYBL1+	
055ACC	55	Male	Primary	Base of tongue	Cribriform/Tubular	+	
057ACC	67	Female	Primary	Parotid gland	Cribriform/Tubular	-	
062ACC	49	Female	Primary	Base of tongue	Cribriform/Tubular	+	
064ACC	89	Female	Primary	Buccal mucosa	Solid	+	
065ACC	61	Female	Primary	Parotid gland	Cribriform/Tubular	+	
066ACC	62	Female	Primary	Palate	Cribriform/Tubular	+	
068ACC	45	Male	Primary	Submandibular gland	Cribriform/Tubular	-	
069ACC	63	Female	Recurrent	Maxillary sinus	Cribriform/Tubular/Solid (solid <20%)	-	
071ACC	46	Female	Primary	Oropharynx	Cribriform/Tubular	+	
072ACC	56	Male	Recurrent	Palate	Solid	+	
073ACC	49	Male	Primary	Palate	Cribriform/Tubular	+	
074ACC	74	Female	Primary	Maxillary sinus	Cribriform	+	
076ACC	39	Male	Primary	Palate	Solid	+	
077ACC	56	Male	Primary	Palate	Cribriform/Tubular	MYBL1+	

Establishment of PDXs of ACC and pre-clinical efficacy of combination therapy
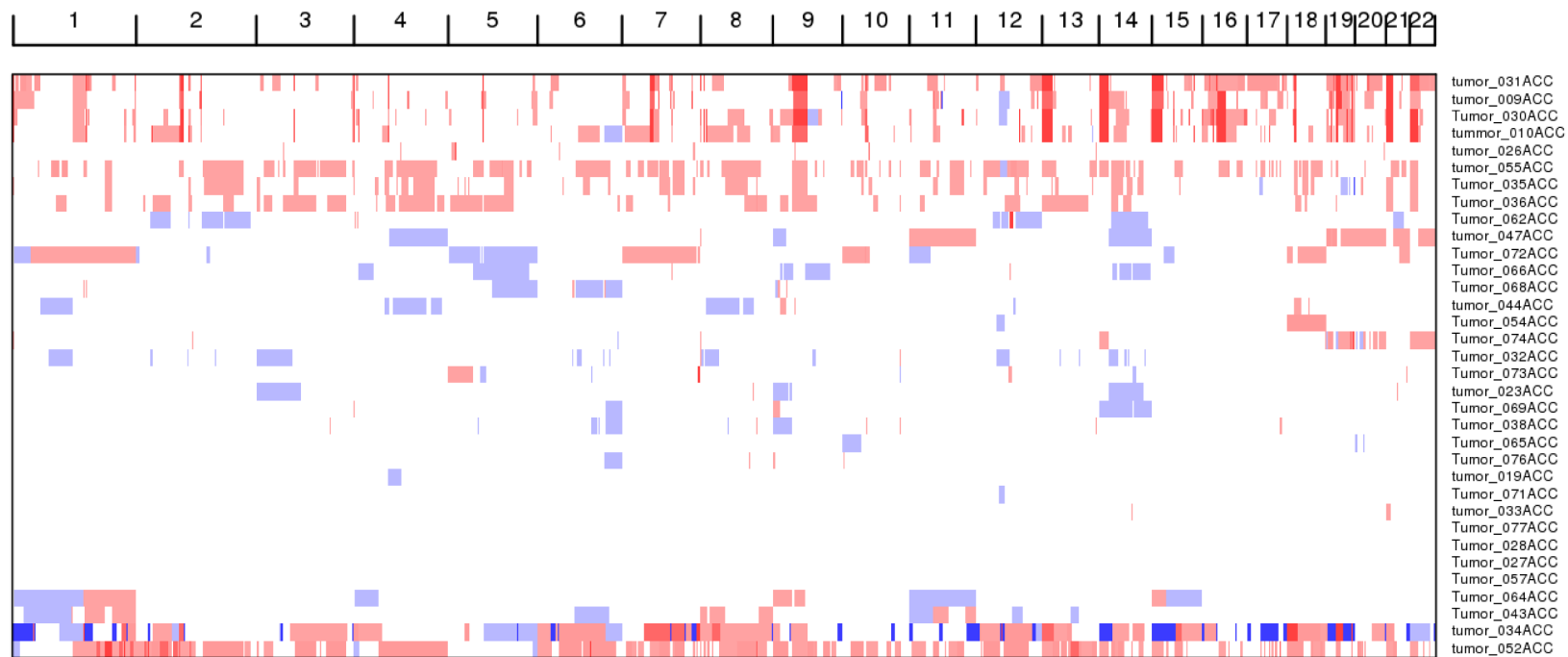
Figure S1. Mutation spectrum and mutational signature. A. Mutation spectrum. The different colors represent 6 different mutation types. B. Mutational signature. The mutation types of ACC samples were clustered by the nonnegative matrix factorization (NMF) algorithm, and each mutation characteristic represented one or more tumor mutation processes. C. CNVs in 34 ACC tumors.
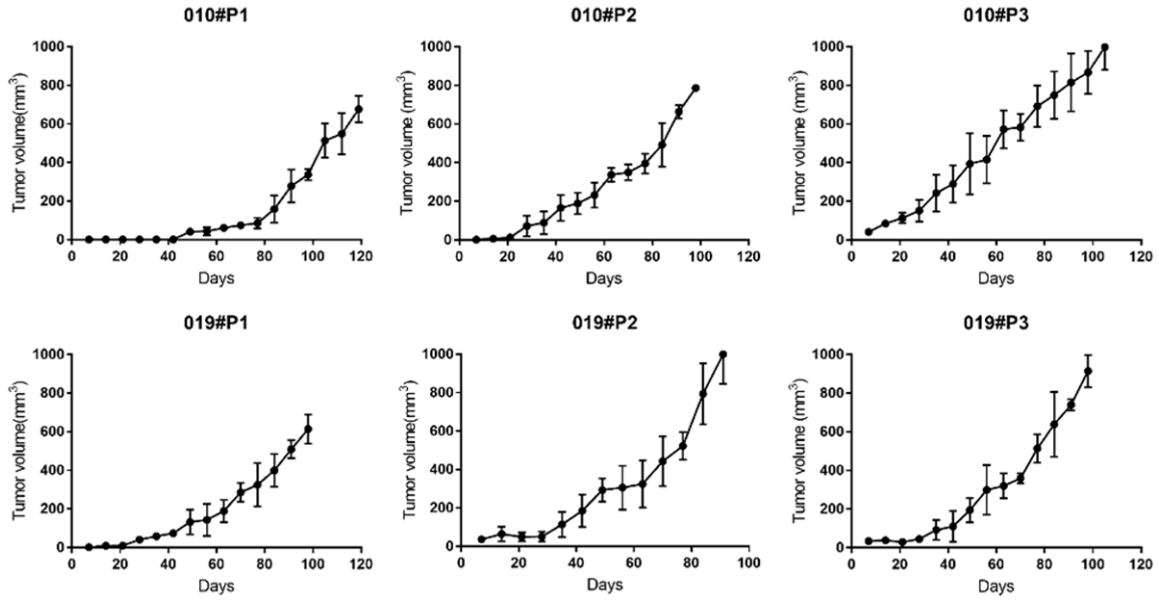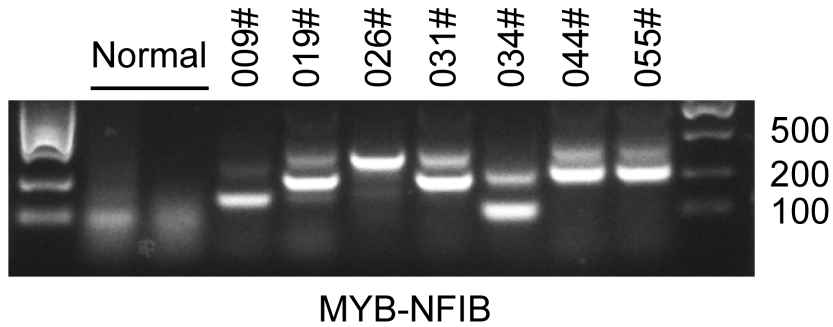
Figure S2. Growth curve of PDXs from P1 to P3. 010-ACC and 019-ACC PDX growth curve are shown. P1-P3 (passage 1 to passage 3). The x-axis indicates time and the Y-ordinate showed tumor volume.

Figure S3. Identification of fusion genes. A. MYB-NFIB in several ACC tumors were verified by RT-PCR. B-D. RNA-seq analysis identified the fusion gene NFIB-MAP3K5 in one ACC patient sample and PDX. NFIB-MAP3K5 gene fusion product was verified by RT-PCR and Sanger sequencing.

Figure S4. Mutation burden and SNVs in ACC patient tumors and PDXs. A, B. TMB and gene spectrum of ACC patient tumors and PDXs. C. G-scores of ACC patient tumors and PDXs.